Full counting statistics of spin-flip and spin-conserving charge transitions in Pauli-spin blockade

Sadashige Matsuo,[1,2,3,*,†] Kazuyuki Kuroyama,[1,2,*,‡] Shunsuke Yabunaka,[4] Sascha R. Valentin,[5] Arne Ludwig,[5] Andreas D. Wieck,[5] and Seigo Tarucha[1,2,§]

[1]Department of Applied Physics, the University of Tokyo, 7-3-1 Hongo, Bunkyo-ku, Tokyo 113-8656, Japan
[2]Center for Emergent Matter Science, RIKEN, 2-1 Hirosawa, Wako-shi, Saitama 351-0198, Japan
[3]JST, PRESTO, 4-1-8 Honcho, Kawaguchi, Saitama 332-0012, Japan
[4]Department of Physics, Kyushu University, Fukuoka 819-0395, Japan
[5]Lehrstuhl für Angewandte Festkörperphysik, Ruhr-Universität Bochum, D-44780 Bochum, Germany

(Received 26 September 2019; revised 21 June 2020; accepted 24 June 2020; published 22 July 2020)

We investigate the full counting statistics (FCS) of spin-conserving and spin-flip charge transitions in Pauli-spin blockade regime of a GaAs double quantum dot. Experimentally, we executed real-time observation of charge transitions and constructed the FCS. A theoretical model is proposed to evaluate all spin-conserving and spin-flip tunnel rates. We enumerate advantages in FCS comparing to waiting time distribution for the evaluation with demonstration of the universal relation between FCS and waiting time distribution We report peculiar statistical features in the FCS, which appear in the system holding spin degeneracy and coexistence of slow and fast transitions. Our experimental results supported by the numerical calculation provide how the spin correlation plays on the full counting statistics. This study is potentially useful for elucidating the spin-related and other complex transition dynamics in classical and quantum systems.

DOI: 10.1103/PhysRevResearch.2.033120

I. INTRODUCTION

The recent advances in charge sensing technologies using single electron transistors or quantum dots (QDs) have facilitated the tracking of charge dynamics, including charge tunneling, electron-phonon coupling, and generation of photoelectrons with the resolution of single charge [1–8]. Such charge dynamics can be used to reveal the microscopic mechanism of statistical or thermodynamical phenomena, such as the fluctuation theorem [9–11] and Maxwell demon engine [12,13]. QDs have been extensively utilized as a tunable platform for investigating and controlling these phenomena. Full counting statistics (FCS) is one of the most effective tools to analyze the charge dynamics, which yields the probability density $p(n, t)$ of n transitions in a time window t. FCS encodes all the cumulants, which include not only the mean but also the fluctuations and higher-order correlations [14,15]. Consequently, it has been used for investigating the cumulant asymmetry [16], super-Poissonian properties and the spin relaxation [17], and universal oscillation of the higher-order cumulants [18] in a single QD, bidirectional counting and antibunching correlation in a double QD (DQD) [19], avalanche of the Andreev reflection events [20], and optically detected single-electron tunneling [21]. However, experimental demonstration of FCS has been limited to QDs with just a few internal degrees of freedom. In order to establish FCS for more complicated statistical phenomena, it is necessary to investigate QDs with more internal degrees of freedom, e.g., spin-related coupling between quantum states, or coexisting fast and slow transitions.

Such complicated phenomena in mesoscopic devices on which the spin effect plays significant roles have been intensively studied in several research fields. Since the late 2000s, the development of spintronics in mesoscopic devices is remarkable. For example, generation of spin current due to spin-orbit interaction has been detected in semiconductor devices [22,23]. Studies on the charge and spin statistics of such phenomena will reveal the microscopic dynamics of the charge-spin conversion and improve the conversion rate. Additionally, the statistics in spintronic devices is strongly related to the thermodynamical properties so that the statistics will also contribute to establishing the spin caloritronics [24]. Furthermore, quantum natures of spins in electrical devices are now controllable as represented by qubit operations in semiconductor QDs. Technology development will enable to emulate the Fermi-Hubbard model in integrated QD devices [25] in which ferromagnetism [26–29] and high-temperature superconductivity [30,31] would emerge. Therefore, revealing universal statistical properties and establishment of evaluation methods of the spin-correlated phenomena in a few coupled QDs will pave the way to elucidate the charge and spin dynamics such as thermal or quantum fluctuation of spins in the important phenomena in condensed matter physics.

In this work, we choose the Pauli-spin blockade (PSB) effect in a DQD [32] to investigate the charge and spin

*These authors contributed equally to this work.
†sadashige.matsuo@riken.jp
‡kuroyama@iis.u-tokyo.ac.jp
§tarucha@riken.jp

dynamics because PSB is the simplest but most significant spin-correlated phenomenon that affects the electron dynamics in a DQD. Real-time charge sensing of a DQD holding two electrons in PSB has been reported in earlier studies, which showed that the charge transitions can be classified into spin-flip and spin-conserving transitions [33–35]. The spin-conserving transitions only occur when the two spins are antiparallel, while the spin-flip transitions change the spin configuration. Consequently, the spin configuration can be different even if the charge state is the same. This additional degree of freedom complicates the charge dynamics.

Here we provide the efficacy of FCS method and peculiar statistical features in the representative spin-correlated phenomenon, PSB. We construct the FCS experimentally and validate it theoretically using our model, which is used to derive all the necessary tunnel rates. Then we demonstrated the relation between FCS and the waiting time distribution (WTD), which allows us to construct WTD even with less amount of measurement data than that necessary to construct the WTD without the relation. This means that all of the information derived from WTD is compiled as a part of FCS so that the use of FCS is more seminal. The observed features in FCS of asymmetric tailing and parity effect, are then discussed in a convincing manner. These findings are potentially useful for understanding more complicated transition dynamics realized in multiple spin-correlated QDs. Furthermore, we suppose that our results on the charge and spin dynamics will be beneficial not only for QDs but also for any other systems in which charge and spin degrees of freedom are well defined. Indeed FCS of spin-flip and spin-conserving tunnels has recently been studied in the research field of cold atoms [36].

II. EXPERIMENTAL CONSTRUCTION OF FULL COUNTING STATISTICS IN PAULI-SPIN BLOCKADE REGIME

For constructing the FCS, we experimentally obtained the real-time traces of charge transitions in the DQD in PSB. The DQD was made in a GaAs quantum well. A scanning electron microscope (SEM) image of this DQD is shown in Fig. 1(b). Here, the target DQD is represented by yellow circles. We applied negative voltages on the gate electrodes indicated as L, C, R, TL, T, and TR, and tuned the DQD in resonance with the transition between (1,1) and (0,2) (see Appendix A). Here (0,2) indicates no electrons in the left QD and two electrons in the right QD. Subsequently, we formed another QD (blue circle) as a charge sensor connected to the high-frequency resonance circuit. We measured real-time traces of the charge sensor response V_{rf} to probe the charge state. A typical real-time trace is shown in Fig. 1(c). V_{rf} exhibits almost binary values of -0.10 and -0.12, indicating the charge state of (0,2) and (1,1), respectively. Therefore, the transitions between these two values indicate the interdot charge transitions.

The FCS of interdot charge transitions can be constructed from the acquired time traces. First, the raw traces are divided into many shorter time traces (time domains) with a span of t. Subsequently, the number of interdot transitions are counted in each time domain. For example, five time domains of

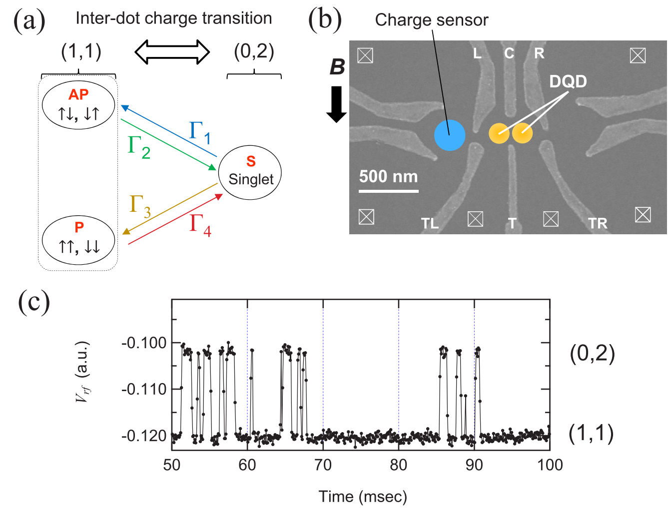

FIG. 1. (a) Schematic diagram for tunneling events of a DQD in PSB. The possible spin configurations of (1,1) charge state are spin antiparallel (AP) and spin parallel (P). The (0,2) charge state is spin-singlet (S). All the three possible states are connected by transitions with rates Γ_1, Γ_2, Γ_3, and Γ_4. (b) Scanning electron microscopy (SEM) image of our DQD. The DQD and charge sensor QD are represented as yellow and blue circles, respectively. (c) Typical time trace of V_{rf}. The jumps in V_{rf} imply the interdot charge transitions between (1,1) and (0,2).

$t = 10$ ms duration can be created in Fig. 1(c). There are 10 transitions between 50 and 60 ms. Finally, we estimate the probability density $p(n, t)$ from the number of time domains with n transitions. On the other hand, WTD is acquired by count of the residence events with the same residence time on a certain charge states.

These constructed FCSs with $t = 10$ and 50 ms and $B = 100$ mT are shown in Fig. 2. Here we find two remarkable features that are not observed in Poisson distribution, $(\Gamma t)^n e^{-\Gamma t}/n!$, which is represented by triangles with a single tunnel rate Γ of 1.28 kHz (only for comparison). First, the obtained FCS has a tail structure at lower n. Second, a parity effect is evident about n; even n exhibits higher probability than odd n. To confirm that these two peculiar features

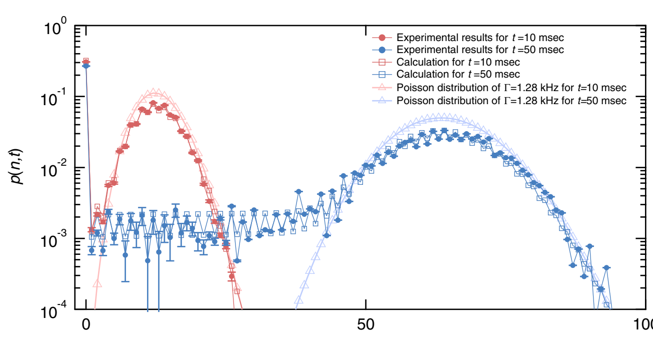

FIG. 2. FCS in PSB. The red and blue circles (triangles) show the experimental (theoretical) results for $t = 10$ and 50 ms, respectively. The red and blue triangles indicate the Poisson distribution with $\Gamma = 1.28$ kHz.

originate from the electron dynamics and not from artifacts such as measurement noise, it is necessary to validate the experimental results with theoretical calculations.

III. THEORETICAL MODEL AND EVALUATION OF THE SPIN-FLIP AND SPIN-CONSERVING TUNNEL RATES

To this end, we now introduce our theoretical model and apply it on the interdot transitions between (0,2) and (1,1) in PSB. The ground states on PSB at a weak magnetic field are enumerated as S(0,2), S(1,1), $T_0(1,1)$, $T_-(1,1) = \downarrow\downarrow(1,1)$, and $T_+(1,1) = \uparrow\uparrow(1,1)$. The spin-conserving resonant tunnels occur between S(0,2) and S(1,1). In addition, ΔE_n, difference of the nuclear Overhauser field between two quantum dots mixes the S(1,1) and $T_0(1,1)$ and the typical precession time is 100 ns derived from $\hbar/\Delta E_n$ [37]. We used 100 μs as the integration time of our digitizer for the real-time measurement. This integration time is much larger than 100 ns. Therefore, we can assume that S(1,1) and $T_0(1,1)$ are treated classically as $\downarrow\uparrow(1,1)$ and $\uparrow\downarrow(1,1)$. Furthermore, Zeeman energy between $T_-(1,1)$ and $T_+(1,1)$ is given as $E_z = g\mu_B B = 1.2\ \mu$eV with g factor of 0.21 and $B = 100$ mT. This is sufficiently smaller than the thermal energy of $k_B T \simeq 10\ \mu$eV. Therefore, we can ignore the Zeeman splitting and identify $T_-(1,1)$ and $T_+(1,1)$ as spin-parallel states P(1,1). Validity of these assumptions has already been proved in the previous studies of the real-time measurement in PSB [33–35].

Now the spin-conserving interdot charge transitions are allowed when the two electrons have opposite spins, but they are prohibited due to the Pauli exclusion principle when the two spins are parallel, and only the spin-flip transitions are allowed in this case. Consequently, we classify (1,1) into antiparallel [AP(1,1)] and parallel [P(1,1)] states of possible spin configurations. Now high-energy excitations are absent, and we are only concerned with the bound state (0,2) whose spin configuration is spin-singlet [S(0,2)]. We define four tunnel rates as Γ_1, Γ_2, Γ_3, and Γ_4 between such possible states. The transition diagram is schematically shown in Fig. 1(a), where Γ_1 and Γ_2 are the spin-conserving tunnel rates, and Γ_3 and Γ_4 are the spin-flip rates.

We define $p_P(n,t)$, $p_{AP}(n,t)$, and $p_S(n,t)$ as the FCS of finding the final state as P(1,1), AP(1,1), and S(0,2) after n transitions during the time span $[0,t]$, respectively. The momentum generation function is $P(\chi,t) = \sum_{n=0}^{\infty}(p_S(n,t)e^{in\chi}, p_{AP}(n,t)e^{in\chi}, p_P(n,t)e^{in\chi})^\tau$, where τ stands for transpose of a vector and χ represents the counting field [20]. We assume that the transition follows a Markovian dynamics. The time evolution equation of $P(\chi,t)$ can therefore be expressed as

$$\frac{dP(\chi,t)}{dt} = \mathcal{M}P(\chi,t) = \begin{bmatrix} -(\Gamma_1+\Gamma_3) & \Gamma_2 e^{i\chi} & \Gamma_4 e^{i\chi} \\ \Gamma_1 e^{i\chi} & -\Gamma_2 & 0 \\ \Gamma_3 e^{i\chi} & 0 & -\Gamma_4 \end{bmatrix} P(\chi,t). \quad (1)$$

It may be noted that the experimental result in Fig. 2 corresponds to the case: $p(n,t) = p_S(n,t) + p_{AP}(n,t) + p_P(n,t)$.

All the tunnel rates should be estimated to theoretically construct the FCS. The FCS with $n = 0$ is available to evaluate the tunnel rates because the probability densities with $n = 0$ consist of time domains including no charge transitions and are equivalent to the idle time distributions. We now focus on $p_S(0,t)$ and $p_{AP}(0,t) + p_P(0,t)$ because the charge state of either (0,2) or (1,1) can be detected. The time evolution of probability distributions obeys Eq. (1) with $e^{i\chi}$ replaced by 0. Therefore, we obtain

$$\begin{bmatrix} p_S(0,t) \\ p_{AP}(0,t) \\ p_P(0,t) \end{bmatrix} = \begin{bmatrix} \frac{\Gamma_2\Gamma_4}{\Gamma_1\Gamma_4+\Gamma_2\Gamma_4+\Gamma_2\Gamma_3} e^{-(\Gamma_1+\Gamma_3)t} \\ \frac{\Gamma_1\Gamma_4}{\Gamma_1\Gamma_4+\Gamma_2\Gamma_4+\Gamma_2\Gamma_3} e^{-\Gamma_2 t} \\ \frac{\Gamma_2\Gamma_3}{\Gamma_1\Gamma_4+\Gamma_2\Gamma_4+\Gamma_2\Gamma_3} e^{-\Gamma_4 t} \end{bmatrix}. \quad (2)$$

First, we estimate Γ_2 and Γ_4 as the exponents in $p_{AP}(0,t) + p_P(0,t)$. Subsequently, we can derive Γ_1 and Γ_3 from the coefficient ratio of the two exponential functions, $\Gamma_1\Gamma_4/\Gamma_2\Gamma_3$ in $p_{AP}(0,t) + p_P(0,t)$ and the exponent, $\Gamma_1 + \Gamma_3$ in $p_S(0,t)$. Consequently, we can estimate all the tunnel rates including Γ_3.

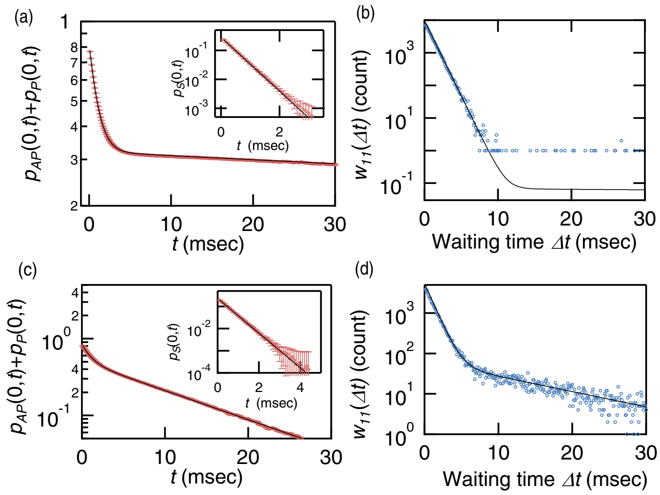

FIG. 3. Evaluation of tunnel rates. (a) $p_{AP}(0,t) + p_P(0,t)$ is represented by the red circles. Inset shows $p_S(0,t)$. The numerical fitting results are denoted by the black curves. (b) Blue circles represent $w_{11}(\Delta t)$ as a histogram of the residence time Δt, which is evaluated from the real-time traces. The black curve indicates the numerical result from $p(0,t)$ and the universal relation between FCS and WTD. Panels (c) and (d) represent the same functions as (a) and (b) for different tunnel rates, respectively.

We now evaluate $p_S(0,t)$ and $p_{AP}(0,t) + p_P(0,t)$ from the time traces shown in Fig. 3(a). Here the solid lines represent the fitting results obtained by Eq. (2), which are in excellent agreement with the experimental results. Consequently, all the tunnel rates can be determined as $(\Gamma_1, \Gamma_2, \Gamma_3, \Gamma_4) =$ (1.873 kHz, 0.976 kHz, 5.10 Hz, 3.51 Hz). We note that the previous studies did not evaluate Γ_3 because they focused on the exponents and not on the coefficients. $\Gamma_1/\Gamma_2 = 2$ due to the spin degeneracy [$\uparrow\downarrow(1,1)$ and $\downarrow\uparrow(1,1)$] of AP(1,1) as previously reported [33,38].

Unlike the spin-conserving rates, we can obtain $\Gamma_3/\Gamma_4 = 1.45$ for the spin-flip rates. This ratio implies that there is an unintentional energy offset from the resonance condition. This is because when these two tunnel rates are equal, the detailed balance condition implies $\Gamma_3/\Gamma_4 = 2\cosh(\Delta E_z/k_B T) \geqslant 2$, where ΔE_z, k_B, and T are the Zeeman energy, Boltzmann

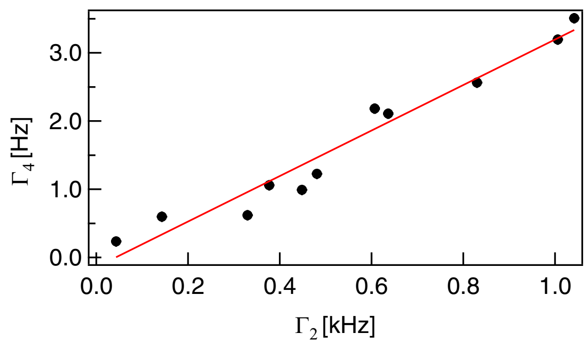

FIG. 4. Γ_4 as a function of Γ_2. For varying Γ_2 and Γ_4, we changed the interdot coupling by controlling the gate voltage (not by the phonon irradiation). Γ_4 is proportional to Γ_2, indicating that the spin-flip is dominantly caused by the spin-orbit interactions and not by the hyperfine interactions.

constant, and temperature, respectively (see Appendix A). We note that the experimental results indicate a clear double exponential function, which guarantees validity of our assumption that we identify $T_-(1,1)$ and $T_+(1,1)$ as spin-parallel states P(1,1). If the two spin-parallel states have the different tunnel rates to S(0,2), then $p(0,t)$ for the (1,1) charge state should be a triple exponential function.

IV. DOMINANT SPIN-ORBIT INTERACTION FOR THE SPIN-FLIP TRANSITIONS

It is important to understand the dominant mechanism for the spin-flip tunnels because the spin-flip originated from the spin-orbit interaction occurs in the interdot process, while that from the hyperfine interaction occurs in the intradot process [33–35]. To this end, we have plotted Γ_4 vs. Γ_2 at different interdot couplings in Fig. 4. It is evident that Γ_4 is proportional to Γ_2, which implies that the spin-flip tunnel is originated from the spin-orbit interaction because the theory predicts that $\Gamma_4 = d^2/2l_{SO}^2\Gamma_2$. d and l_{SO} represent the distance between the two QDs and the spin-orbit length, respectively [35,39]. On the other hand, Γ_4 is expected to be constant as a function of Γ_2 in the hyperfine interaction case. When we assume that the hyperfine interaction is responsible for the spin-flip process, FCS analysis gives $\Gamma_{P(1,1)\to AP(1,1)}/\Gamma_{AP(1,1)\to P(1,1)} \approx 3$ (see Appendix B). However, this result conflicts with theoretical prediction that $\Gamma_{P(1,1)\to AP(1,1)}/\Gamma_{AP(1,1)\to P(1,1)} \approx 1$. Therefore, we ignore the intradot spin-flip processes caused by the hyperfine interaction and adopt the transition diagram shown in Fig. 1(a).

V. RELATION BETWEEN FULL COUNTING STATISTICS AND WAITING TIME DISTRIBUTION

We focus on WTD for (1,1) charge state, $w_{11}(\Delta t)$. We introduce the relation described as $w_{11}(\Delta t) \propto d^2[p_{AP}(0, \Delta t) + p_P(0, \Delta t)]/d(\Delta t)^2$. This relation, in which WTD is proportional to the second derivative of FCS with $n = 0$, is universally established between FCS with $n = 0$ and WTD [40–42] (see Appendix C). From this relation, we can derive $w_{11}(\Delta t) \propto \Gamma_1\Gamma_2 e^{-\Gamma_2\Delta t} + \Gamma_3\Gamma_4 e^{-\Gamma_4\Delta t}$. The histogram of Δt [proportional to $w_{11}(\Delta t)$] is shown as blue circles in Fig. 3(b). The histogram exhibits unity or zero values for $\Delta t > 10$ ms, namely the number of the residence events with $\Delta t > 10$ ms is 1 or 0. This indicates that the number of the events is not sufficient to correctly construct WTD in $\Delta t > 10$ ms. The black line in Fig. 3(b) shows the calculated $w_{11}(\Delta t)$ from the FCS result shown in Fig. 3(a) and the universal relation between FCS with $n = 0$ and WTD. It is confirmed that the experimental WTD does not follow the black line in $\Delta t > 10$ ms.

The results mean that a long data acquisition time is needed for the accurate estimation of Γ_3 and Γ_4 with WTD because the residence time in the blocked state P(1,1) is very long. However when difference between Γ_2 and Γ_4 is large, the measurement setup has difficulty in storing sufficiently long time traces including the long staying events at P(1,1) between the transitions of (0,2) $\to$ (1,1) and (1,1) $\to$ (0,2) while tracking the fast spin-conserving transitions. In our case, a length of the time traces is 1 s. A ratio of residence on S(0,2) is 1/5 derived from four states degenerating in (1,1) and no degeneracy in (0,2). The spin-flip transitions result in the blockade state P(1,1) with $\Gamma_3 = 5.1$ Hz. Then we roughly expect only a single blockade event in a single time trace. The ratio of coefficients for the two exponential functions in $w_{11}(\Delta t)$, i.e., $\Gamma_3\Gamma_4/\Gamma_1\Gamma_2 << 1$ is much smaller than the ratio $\Gamma_1\Gamma_4/\Gamma_2\Gamma_3 \approx 2$ in $p_{AP}(0,t) + p_P(0,t)$. Therefore, the required measurement time to guarantee the evaluation accuracy is longer for WTD than for FCS with $n = 0$. From the above reason, analysis with FCS of $n = 0$ has an advantage in evaluation of the fast and slow transition rates.

We obtained the values of $p_{AP}(0,t) + p_P(0,t)$, $p_S(0,t)$, and $w_{11}(\Delta t)$ at different tunnel rates $(\Gamma_1, \Gamma_2, \Gamma_3, \Gamma_4) = (1.58\text{ kHz}, 0.955\text{ kHz}, 236\text{ Hz}, 87.7\text{ Hz})$, which are shown in Figs. 3(c) and 3(d). The WTD derived from the FCS with $n = 0$ using the universal relation, which is shown as the black line in Fig. 3(d), is in complete agreement with the experimentally obtained histogram. This means that both FCS and WTD are available when the spin-flip rates Γ_3 and Γ_4 are large enough. In addition, the nice agreement in Fig. 3(d) demonstrates the universal relation between FCS with $n = 0$ and WTD. This demonstration implies that FCS with $n = 0$ and the relation allow to reproduce the WTD without a long measurement time for storing the traces.

VI. NUMERICAL RESULTS OF FULL COUNTING STATISTICS AND AN ORIGIN OF THE TAIL STRUCTURE

Finally, we calculate the FCS including $n(\neq 0)$ with the estimated tunnel rates based on Eq. (1), which yields $P(\chi,t) = e^{\mathcal{M}t}P_0$. P_0 is probability with the stationary condition, which is calculated from Eq. (1) with $dP(\chi,t)/dt = 0$ and $\chi = 0$. This results in Eq. (2) with $t = 0$. The open squares in Fig. 2 are the calculation results using the estimated rates in Fig. 3(a) (see Appendix D and E). It is evident that the numerical simulations reproduce the experiments perfectly, including the lower n tail structure and the parity effect. This agreement validates that our model based on FCS explains the transition dynamics of spin-flip and spin-conserving transitions in PSB. It further indicates that the tail structure and the parity effect in Fig. 2 are originated from the electron dynamics. Therefore, we have to establish these physical origins.

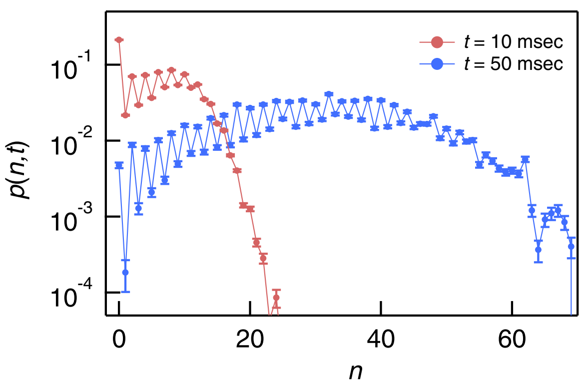

FIG. 5. FCS with the large spin-flip transition rates. The lower n tail has more population than that observed in Fig. 2.

VII. THE LOWER n TAIL ORIGINATED FROM THE COEXISTENCE OF FAST AND SLOW TRANSITIONS

First, the lower n tail is derived from the slow spin-flip rates. As indicated by Eq. (2), $p_S(0,t)$ and $p_{AP}(0,t)$ rapidly decay with t as compared to $p_P(0,t)$. This implies that many spin-conserving transitions occur even in the small span t, while the spin-flip transitions occur rarely. Here the time domains that contain the spin-conserving transitions contribute to the peak at large n, and those containing the finite spin-flip transitions in addition to the spin-conserving transitions contribute to the long slope at smaller n.

This is also supported by the FCS result at fast spin-flip rate. Figure 5 shows the FCS with the similar spin-conserving rates but larger spin-flip rates than the rates used for Fig. 2: $(\Gamma_1, \Gamma_2, \Gamma_3, \Gamma_4) = (1.58\text{ kHz}, 0.955\text{ kHz}, 236\text{ Hz}, 87.7\text{ Hz})$. It is clear that the population at lower n is larger than that in Fig. 2.

Besides, we constructed the FCS at $B = 0$ mT to eliminate the difference of the spin-conserving and spin-flip transition rates. The constructed FCS is shown as circles in Fig. 6. Compared to Fig. 2 and Fig. 5, the parity effect is retained, but the tail at lower n vanishes. These FCS results support our conclusion that the slow spin-flip tunnels are responsible for the observed tail structure at lower n.

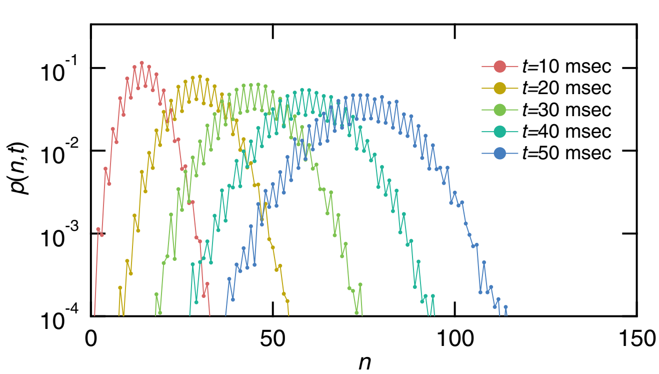

FIG. 6. FCS obtained at $B = 0$ T with several time windows t. The parity effect is retained, but the tail at lower n vanishes.

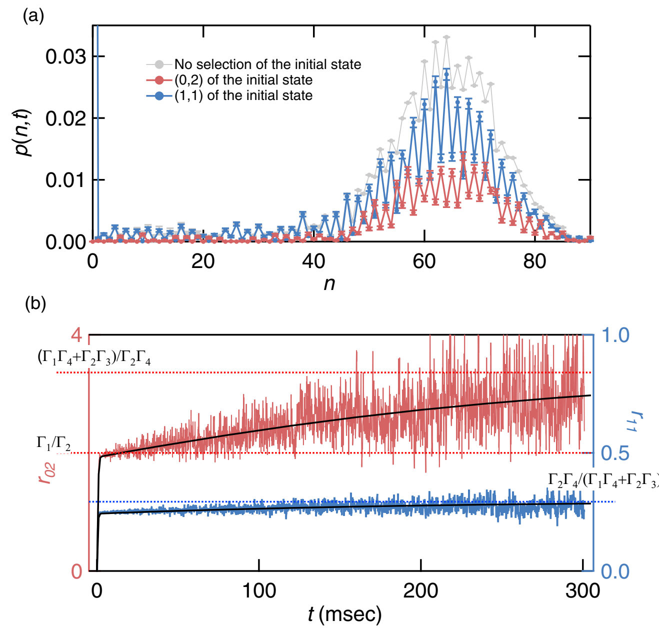

FIG. 7. (a) FCS with and without the selection of the initial state. The gray circles indicate FCS without selection, while the blue and red circles indicate FCS with (0,2) and (1,1) as the initial state, respectively. The parity effect reverses for the different initial states. (b) The red and blue lines represent the ratio of the odd n probability to the even n probability for the (0,2) and (1,1) initial states, respectively. The black lines show the calculated results based on our theoretical model.

VIII. THE PARITY EFFECT ORIGINATED FROM THE DEGENERACY

We reconstructed the FCS of the time domains with the same initial states to elucidate the origin of the parity effect. The red and blue circles in Fig. 7(a) indicate the FCS constructed using the time domains with the initial state as (0,2) and (1,1) with $t = 50$ ms, respectively. The gray circles are equivalent to the blue circles in Fig. 2. It is evident here that the parity effect on the red circles is opposite to that on the blue ones. This can be understood in terms of the equilibration of the initial states. The selected initial state, i.e., (0,2) or (1,1) is equilibrated into the (0,2) and (1,1) states after a long time with probabilities $\frac{\Gamma_2\Gamma_4}{\Gamma_1\Gamma_4+\Gamma_2\Gamma_4+\Gamma_2\Gamma_3} \approx 1/5$ and $\frac{\Gamma_1\Gamma_4+\Gamma_2\Gamma_3}{\Gamma_1\Gamma_4+\Gamma_2\Gamma_4+\Gamma_2\Gamma_3} \approx 4/5$, respectively. Then, the charge state tends to be (1,1) rather than (0,2) due to the higher spin degeneracy in (1,1). Herein, the probability of odd n becomes larger for the initial state (0,2) because the (0,2) state evolves to (1,1) after the odd n transitions. On the contrary, the probability of even n becomes larger when the initial state is (1,1), resulting in an opposite parity effect to the case with (0,2) as the initial state. The parity effect in FCS with no initial state selection is dominated by (1,1) initial state because the corresponding probability is larger than that for the (0,2) case, as seen in Fig. 3(a).

We note that the FCS at $B = 0$ mT in Fig. 6 also shows the parity effect because the spin degeneracy in (1,1) remains at $B = 0$ mT.

The time evolution of the parity effect can be explained in terms of r_{02} and r_{11}, defined as

$$\frac{\sum_{m=0}^{\infty} p_S^i(2m+1,t)}{\sum_{m=0}^{\infty} p_S^i(2m,t)}$$

$$\text{and } \frac{\sum_{m=0}^{\infty}[p_{AP}^i(2m+1,t)+p_P^i(2m+1,t)]}{\sum_{m=0}^{\infty}[p_{AP}^i(2m,t)+p_P^i(2m,t)]},$$

which are plotted as blue and red lines in Fig. 7(b), respectively. Here we define $p_j^i(n,t)$ as the FCS with the selected initial state j (j = S, AP, or P). The numerical calculations (black lines) are in excellent agreement with the experiments. r_{02} approaches Γ_1/Γ_2 around $t = 1$ ms $\approx 1/\Gamma_2$, and then it becomes $(\Gamma_1\Gamma_4+\Gamma_2\Gamma_3)/\Gamma_2\Gamma_4$ around $t \approx 1/\Gamma_4$. This is because the spin-conserving tunnels between (0,2) and AP(1,1) occur initially due to the larger rate. Then the spin-flip tunnels generate the transitions between (0,2) and P(1,1) with the smaller rates. r_{11} evolves as $\Gamma_2\Gamma_4/(\Gamma_1\Gamma_4+\Gamma_2\Gamma_3)$. Such time evolution reflects the equilibration of the initial state, which finally saturates at the ratio corresponding to the equilibrium condition.

IX. CONCLUSION

In conclusion, we study the FCS of spin-conserving and spin-flip charge transitions in PSB. We indicate the advantages of FCS comparing to WTD when we analyze the tunnel rates. We demonstrate the universal relation between FCS and WTD, which means that WTD can be reproduced from FCS with $n = 0$ even if a measurement time is short. We constructed the FCS and found two peculiar features: the tail structure and parity effect, which are derived from the slow spin-flip tunnel rates and higher spin degeneracy, respectively. Our results provide a powerful tool and insights for understanding the complex transition dynamics of such as spin-correlated phenomena in the Hubbard model emulated in the integrated QDs. Herein, our finding and the FCS method presented here will be a key ingredient for evaluation of charge and spin dynamics in spintronics devices and thermal and quantum fluctuation of charges and spins in the Hubbard model emulated in the integrated QDs.

ACKNOWLEDGMENT

We greatly thank Professor Yasuhiro Tokura for his significant comments. This work was partially supported by the Grant-in-Aid for Scientific Research (B) (Grant No. JP18H01813), the Grant-in-Aid for Scientific Research (S) (Grants No. JP26220710 and No. JP19H05610), the Grant-in-Aid for Early-Career Scientists (Grant No. JP18K13516), JSPS Program for Leading Graduate Schools (ALPS), JSPS Research Fellowship for Young Scientists (Grants No. JP16J03037 and No. JP19J01737), the Grant-in-Aid for Scientific Research on Innovative Area Nano Spin Conversion Science (Grant No. JP17H05177), JST CREST (Grant No. JPMJCR15N2), JST PRESTO (Grant No. JPMJPR18L8), and RIKEN-Kyudai Science and Technology Hub Collaborative Research Program. S.R.V., A.L., and A.D.W. acknowledge gratefully support of DFG-TRR160 (Grant B4) and BMBF - Q.Link.X (Grant No. 16KIS0867).

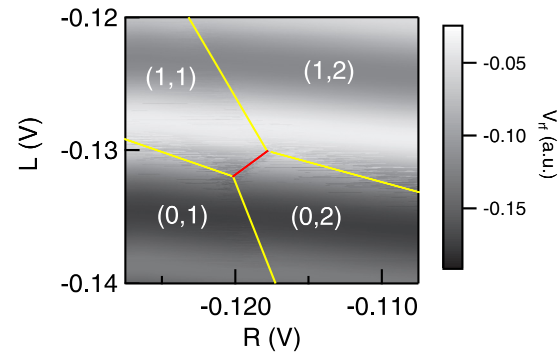

FIG. 8. Stability diagram of DQD around the boundary of (0,2) and (1,1) states. The red line represents the resonance line, which corresponds to the measurement location.

APPENDIX A: MEASUREMENT CONDITION OF A DQD

Figure 8 shows the stability diagram of our DQD as a function of gate voltage. The resonance condition is satisfied at the red line, which appears between the (1,1) and (0,2) states. This measurement was performed for the case in which the spin-conserving tunnel rates were maximum. Therefore, we assumed that the energies of S(0,2), $\downarrow\uparrow(1,1)$, and $\uparrow\downarrow(1,1)$ states are equal. Now the exchange coupling which separates $\downarrow\uparrow(1,1)$ and $\uparrow\downarrow(1,1)$ is much weaker than the measurement temperature and Zeeman energy so that we ignore it.

Unlike the spin-conserving rates, $\Gamma_3/\Gamma_4 = 1.45 \neq 2$ is obtained for the spin-flip rates. This ratio implies that there is an unintentional energy offset δ from the resonance condition in addition to the Zeeman energy ΔE_z, k_B and thermal energy k_BT (k_B and T are the Boltzmann constant, and temperature, respectively). We introduce the probabilities, c_i ($i = S(0,2), \uparrow\uparrow(1,1), \downarrow\downarrow(1,1)$) in the equilibrium condition that the state is found in the charge state represented by i. Then thermal equilibrium condition derives $c_S/c_{\uparrow\uparrow} = \exp[-(E_z+\delta)/k_BT]$ from the Boltzmann distribution. With the same manner, $c_{\downarrow\downarrow}/c_S = \exp[-(E_z-\delta)/k_BT]$ is satisfied. Therefore, ratio in P(1,1) to that in S(0,2) is given as

$$\begin{aligned}\frac{c_{\uparrow\uparrow}+c_{\downarrow\downarrow}}{c_S} &= \exp[(E_z+\delta)/k_BT]+\exp[-(E_z-\delta)/k_BT]\\ &= 2e^{\delta/k_BT}\cosh(E_z/k_BT).\end{aligned}$$

The detailed balance demands $\Gamma_3 c_S = \Gamma_4(c_{\uparrow\uparrow}+c_{\downarrow\downarrow})$, resulting in $\Gamma_3/\Gamma_4 = 2e^{\delta/k_BT}\cosh(E_z/k_BT)$. Then we acquire $\delta = -1.2\ \mu$eV with $T = 100$ mK and $E_z = g\mu_B B/2 = 0.61\ \mu$eV with g factor of 0.21 and $B = 100$ mT.

APPENDIX B: FCS IN VARIOUS CONDITIONS

1. FCS with phonon irradiation

In Figs. 3(c) and 3(d) in the main manuscript, we use the real-time traces in the case of $(\Gamma_1, \Gamma_2, \Gamma_3, \Gamma_4) =$ (1.58 kHz, 0.955 kHz, 236 Hz, 87.7 Hz), where the spin-flip rates comparing to those in Figs. 3(a) and 3(b) are remarkably enhanced while the spin-conserving rates less change. For only increasing the spin-flip rates, we irradiate nonequilibrium phonons on our DQD.

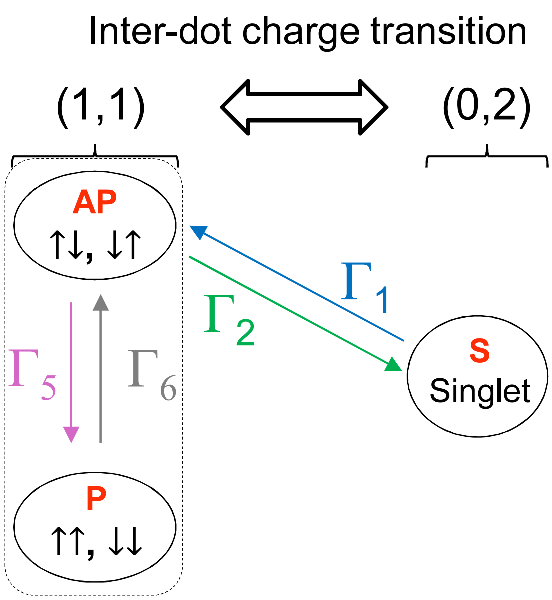

FIG. 9. Transition diagram for the case in which the hyperfine interactions primarily cause the spin-flip transition. In contrast to Fig. 1(a), no spin-flip interdot transition occurs between the P(1,1) and S(0,2) states, and spin-flip intradot transition occurs between the P(1,1) and AP(1,1) states instead.

We formed an additional QD as a phonon source near the DQD in Fig. 1(b). A bias voltage was applied on this phonon source, which caused the inelastic process emitting nonequilibrium phonons. This phonon irradiation resulted in the increase of Γ_3 and Γ_4 with minor change in Γ_1 and Γ_2. This implies that the phonon irradiation selectively accelerates the spin-flip tunnel rates. The details of this method and the underlying mechanism are discussed in another paper.

2. FCS of the spin-flip tunnels from hyperfine interactions

It is important to examine the FCS for the case in which the spin-flip tunnel occurs due to hyperfine interactions. In this case, the charge transition diagram in Fig. 1(a) is converted to that in Fig. 9 because the spin-flip transition is now an intradot process. The probability distributions follow

$$\frac{dP(\chi,t)}{dt} = \begin{bmatrix} -\Gamma_1 & \Gamma_2 e^{i\chi} & 0 \\ \Gamma_1 e^{i\chi} & -(\Gamma_2+\Gamma_5) & \Gamma_6 \\ 0 & \Gamma_5 & -\Gamma_6 \end{bmatrix} P(\chi,t).$$

Using this model, the probability with $n = 0$ can be obtained as

$$\begin{aligned} p_S(0,t) &\propto e^{-\Gamma_1 t} \\ p_{AP}(0,t) + p_P(0,t) &\propto \beta^2\Gamma_5 e^{\alpha t} + (\alpha+\Gamma_2)^2\Gamma_6 e^{\beta t} \end{aligned} \tag{B1}$$

and here we use α and β as

$$\begin{aligned} 2\alpha &= -(\Gamma_2+\Gamma_5+\Gamma_6) + \sqrt{(\Gamma_2+\Gamma_5+\Gamma_6)^2 - 4\Gamma_2\Gamma_6} \\ 2\beta &= -(\Gamma_2+\Gamma_5+\Gamma_6) - \sqrt{(\Gamma_2+\Gamma_5+\Gamma_6)^2 - 4\Gamma_2\Gamma_6}. \end{aligned}$$

For $\Gamma_5, \Gamma_6 << \Gamma_1, \Gamma_2$, Eq. (B1) can be simplified as follows:

$$p_{AP}(0,t) + p_P(0,t) \propto \Gamma_5 e^{-\Gamma_6 t} + \Gamma_6 e^{-\Gamma_2 t}.$$

If this model is chosen for the analysis, then we obtain $\Gamma_6/\Gamma_5 \approx 3$. However, this result is debatable because the AP(1,1) and P(1,1) states consist of two spin states and therefore $\Gamma_6/\Gamma_5 \approx 1$ is expected. This supports that the spin-flip in our device at 100 mT is originated from the spin-orbit interactions, and it occurs during the interdot transition.

APPENDIX C: THE UNIVERSAL RELATION BETWEEN FCS AND WTD

For establishing the relation between FCS and WTD, we utilize a more general scheme with time dependent couting fields $\lambda_{(0,2)\to(1,1)}$ and $\lambda_{(1,1)\to(0,2)}$ which count transitions, at time t, from (0,2) to (1,1) and from (1,1) to (0,2), respectively. We consider $P(\{\lambda_i\},t)$ that satisfies

$$\begin{aligned} \frac{d}{dt}P(\{\lambda_i\},t) &= \begin{bmatrix} -(\Gamma_1+\Gamma_3) & \Gamma_2\lambda_{(1,1)\to(0,2)} & \Gamma_4\lambda_{(1,1)\to(0,2)} \\ \Gamma_1\lambda_{(0,2)\to(1,1)} & -\Gamma_2 & 0 \\ \Gamma_3\lambda_{(0,2)\to(1,1)} & 0 & -\Gamma_4 \end{bmatrix} P(\{\lambda_i\},t) \\ &\equiv \left[M_0 + \sum_{i=(0,2)\to(1,1),(1,1)\to(0,2)} \lambda_i M_i \right] P(\{\lambda_i\},t). \end{aligned}$$

Here we introduce M_0, $M_{(0,2)\to(1,1)}$, and $M_{(1,1)\to(0,2)}$. We note that M_0 is a diagonal matrix.

As the initial states at $t = t_i$, we use c_i ($i =$ S, AP, P), which is obtained from Eq. (2) and

$$\begin{aligned} p_S(0,t) &= c_S e^{-(\Gamma_1+\Gamma_3)t} \\ p_{AP}(0,t) &= c_{AP} e^{-\Gamma_2 t} \\ p_P(0,t) &= c_P e^{-\Gamma_4 t}. \end{aligned}$$

These c_i gives the probabilities in the steady state. Then, we define $P_{\rm st}$ as $P_{\rm st} \equiv (c_S, c_{AP}, c_P)^\tau$. Here τ stands for transposition of a vector. This means that the system is in the steady state at $t = t_i$. In this section, we consider the time evolution of this system up to the final time $t = t_f$.

We evaluate the joint probability of a transition from (0,2) to (1,1) in the interval $[t_i, t_i+\delta t_i]$, no transition in $[t_i+\delta t_i, t_f-\delta t_f]$ and a transition from (1,1) to (0,2) in the interval $[t_f-\delta t_f, t_f]$. In the limit $\delta t_i, \delta t_f \to 0$, the probability is given as

$$
\begin{aligned}
&(1,1,1)M_{(1,1)\to(0,2)}\delta t_f \exp[-M_0(t_f-t_i)]M_{(0,2)\to(1,1)}\delta t_i P_{\rm st} \\
&= (1,1,1)\begin{pmatrix} 0 & 0 & 0 \\ 0 & \Gamma_2 & 0 \\ 0 & 0 & \Gamma_4 \end{pmatrix} \exp[-M_0(t_f-t_i)] \begin{pmatrix} 0 & 0 & 0 \\ 0 & \Gamma_2 & 0 \\ 0 & 0 & \Gamma_4 \end{pmatrix} P_{\rm st}\delta t_i \delta t_f \\
&= (1,1,1)\begin{pmatrix} 0 & 0 & 0 \\ 0 & 1 & 0 \\ 0 & 0 & 1 \end{pmatrix} M_0 \exp[-M_0(t_f-t_i)] M_0 \begin{pmatrix} 0 & 0 & 0 \\ 0 & 1 & 0 \\ 0 & 0 & 1 \end{pmatrix} P_{\rm st}\delta t_i \delta t_f \\
&= \frac{d^2}{d(t_f-t_i)^2}(1,1,1)\exp[-M_0(t_f-t_i)] \begin{pmatrix} 0 & 0 & 0 \\ 0 & 1 & 0 \\ 0 & 0 & 1 \end{pmatrix} P_{\rm st}\delta t_i \delta t_f \\
&= \frac{d^2}{d(t_f-t_i)^2}[p_{AP}(0, t_f-t_i) + p_P(0, t_f-t_i)]\delta t_i \delta t_f.
\end{aligned}
$$

From the first line to the second line, we have used

$$(\Gamma_1, -\Gamma_2, 0)P_{\rm st} = 0,$$
$$(\Gamma_3, 0, -\Gamma_4)P_{\rm st} = 0,$$

which can be shown from the definition of the steady state $[M_0 + M_{(0,2)\to(1,1)} + M_{(1,1)\to(0,2)}]P_{\rm st} = 0$.

On the other hand, from the definition of the waiting time distribution $w_{11}(t_f - t_i)$, the above joint probability is also expressed as

$$w_{11}(t_f-t_i)(c_{AP}\Gamma_2 + c_P\Gamma_4)\delta t_i \delta t_f,$$

since the probability of a transition from (0,2) to (1,1) in the interval $[t_i, t_i+\delta t_i]$ is $(c_{AP}\Gamma_2 + c_P\Gamma_4)\delta t_i$. By comparing the above two expressions, we prove the following relation between WTD and FCS with $n = 0$:

$$
\begin{aligned}
&\frac{d^2}{d(\Delta t)^2}[p_{AP}(0,\Delta t) + p_P(0,\Delta t)] \\
&= (c_{AP}\Gamma_2 + c_P\Gamma_4)w_{11}(\Delta t).
\end{aligned}
$$

Here we represent the resident time $t_f - t_i$ by Δt. We can also express the above formula in a slightly different way [40–42]

$$\langle\tau\rangle \tfrac{d^2}{d(\Delta t)^2}\Pi_{11}(\Delta t) = w_{11}(\Delta t).$$

Here the idle time distribution is defined as $\Pi_{11}(\Delta t) = [p_{AP}(0,\Delta t) + p_P(0,\Delta t)]/(c_{AP} + c_P)$ and the mean waiting time $\langle\tau\rangle$ is defined as $\langle\tau\rangle \equiv (c_{AP} + c_P)/(c_{AP}\Gamma_2 + c_P\Gamma_4)$.

Using this relation between FCS with $n = 0$ and WTD, we obtain

$$w_{11}(\Delta t) \propto \Gamma_1\Gamma_2 e^{-\Gamma_2\Delta t} + \Gamma_3\Gamma_4 e^{-\Gamma_4\Delta t}.$$

APPENDIX D: CORRECTION IN THE EVALUATION OF THE TUNNEL RATES

For the evaluation of Γ_1 and Γ_3, we first fitted $p_S(0,t)$. to obtain the exponent Γ_{02}^* of the single exponential function of $p_S(0,t)$ as

$$\Gamma_{02}^* = \Gamma_1 + \Gamma_3. \tag{D1}$$

However, a second equation is required to evaluate Γ_1 and Γ_3 independently. Using the FCS method, we can derive the following relation between the tunnel rates and the coefficients of the exponential functions obtained from the fitting:

$$\Gamma_3/\Gamma_4 = (c_P/c_{AP})(\Gamma_1/\Gamma_2). \tag{D2}$$

However, when the rates are derived using Eqs. (D1) and (D2), the calculated c_i gives $c_S + c_{AP} + c_P > 1$. This is because when the transitions in a certain time domain occur in either $0 < t < \tau/2$ or $T - \tau/2 < t < T$, they cannot be detected and the time domains are counted for calculation of c_i.

For this compensation, we introduce the survival probability $P_i^s(\Delta t)\,(i = S, AP, P)$ that the charge state remains in S(0,2), AP(1,1), or P(1,1) after Δt. This survival probability obeys

$$dP_S^s(\Delta t)/d\Delta t = -(\Gamma_1 + \Gamma_3)P_S^s(\Delta t), \tag{D3}$$

$$dP_{AP}^s(\Delta t)/d\Delta t = -\Gamma_2 P_{AP}^s(\Delta t), \tag{D4}$$

$$dP_P^s(\Delta t)/d\Delta t = -\Gamma_4 P_P^s(\Delta t). \tag{D5}$$

We consider the probability that a single transition occurs from AP(1,1) to S(0,2) in $0 < t < \tau/2$, and the charge state stays at S(0,2) in $\tau/2 < t < T$. This probability is calculated as the product of the probability that the initial state is found in AP(1,1), the probability that the transition occurs in $0 < t < \tau/2$, and the survival probability in the S(0,2) for $\tau/2 < t < T$ [see Fig. 10(a)],

$$\left|\int_0^{\tau/2} c_{AP}\frac{dP_{AP}^s(\Delta t)}{d\Delta t}P_S^s(T-\Delta t)d\Delta t\right|.$$

It may be noted that c_{AP} provides the volume ratio in the equilibrium condition for AP(1,1). Similarly, the probability for P(1,1) can be obtained as

$$\left|\int_0^{\tau/2} c_P\frac{dP_P^s(\Delta t)}{d\Delta t}P_S^s(T-\Delta t)d\Delta t\right|,$$

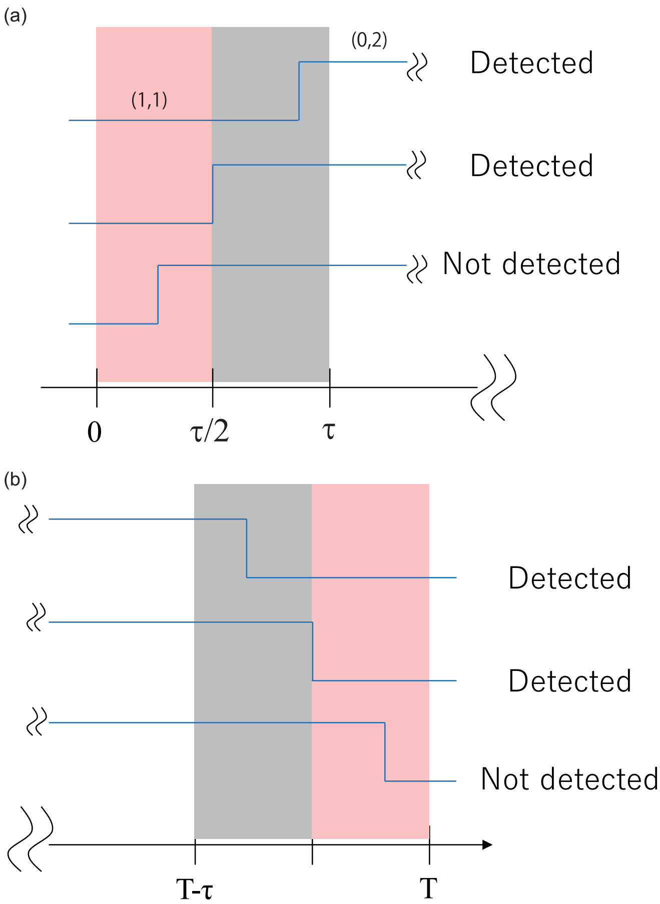

FIG. 10. (a) Interdot transitions from (1,1) to (0,2) states occurring in the first period of $\tau/2$. The first and second cases with the interdot tunnel occurring in the gray region ($\tau/2 < t < \tau$) can be observed in the measured data. On the other hand, the third case, i.e., where the interdot transition occurs in the red region ($0 < t < \tau/2$), cannot be detected. (b) Similarly to (a), an interdot tunnel starting in the red region ($T - \tau/2 < t < T$) cannot be detected.

and the probability that the transition occurs in $T - \tau/2 < t < T$ [see Fig. 10(b)] can be obtained as

$$\Bigg| \int_0^{\tau/2} c_S[\Gamma_1 P_S^s(T-\Delta t)P_{AP}^s(\Delta t) + \Gamma_3 P_S^s(T-\Delta t)P_P^s(\Delta t)]d\Delta t \Bigg|.$$

These probabilities are added to the probability that no transition occurs, which is expressed as $c_S P_S^s(T)$.

Now we obtain $\Gamma_1, \Gamma_3, c_S, c_{AP}$, and c_P from the experimental results including the above compensation. c_S can be expressed as the sum of $p_S^*(0,t) = c_S^* e^{-(\Gamma_1+\Gamma_3)t}$, $p_{AP}^*(0,t) = c_{AP}^* e^{-\Gamma_2 t}$, and $p_P^*(0,t) = c_P^* e^{-\Gamma_4 t}$ so that the following condition is satisfied:

$$\begin{aligned} c_S^* e^{-(\Gamma_1+\Gamma_3)T} &= c_S e^{-(\Gamma_1+\Gamma_3)T} \\ &+ c_{AP}\frac{\Gamma_2}{\Gamma_1+\Gamma_3-\Gamma_2}e^{-(\Gamma_1+\Gamma_3)T}[e^{(\Gamma_1+\Gamma_3-\Gamma_2)\tau/2}-1] \\ &+ c_P\frac{\Gamma_4}{\Gamma_1+\Gamma_3-\Gamma_4}e^{-(\Gamma_1+\Gamma_3)T}[e^{(\Gamma_1+\Gamma_3-\Gamma_4)\tau/2}-1] \\ &+ c_S\frac{\Gamma_1}{\Gamma_1+\Gamma_3-\Gamma_2}e^{-(\Gamma_1+\Gamma_3)T}[e^{(\Gamma_1+\Gamma_3-\Gamma_2)\tau/2}-1] \\ &+ c_S\frac{\Gamma_3}{\Gamma_1+\Gamma_3-\Gamma_4}e^{-(\Gamma_1+\Gamma_3)T}[e^{(\Gamma_1+\Gamma_3-\Gamma_4)\tau/2}-1]. \end{aligned}$$

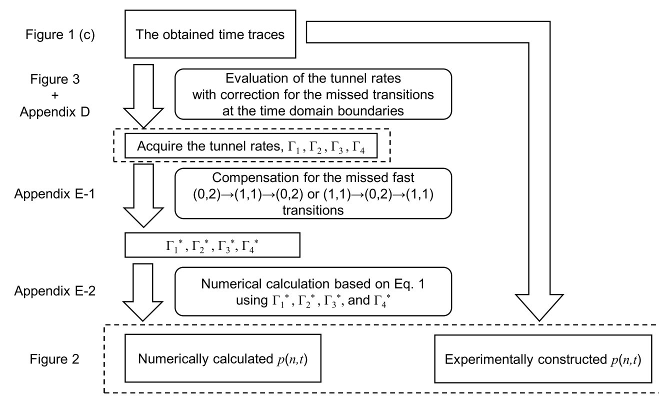

FIG. 11. A flowchart for the numerical calculation of FCS.

The above equation can be simplified as

$$\begin{aligned} c_S^* = c_S &+ \frac{c_{AP}\Gamma_2 + c_S\Gamma_1}{\Gamma_1+\Gamma_3-\Gamma_2}[e^{(\Gamma_1+\Gamma_3-\Gamma_2)\tau/2}-1] \\ &+ \frac{c_P\Gamma_4 + c_S\Gamma_3}{\Gamma_1+\Gamma_3-\Gamma_4}[e^{(\Gamma_1+\Gamma_3-\Gamma_4)\tau/2}-1]. \end{aligned}$$

The equations for the other coefficients can be similarly obtained as

$$\begin{aligned} c_{AP}^* &= c_{AP} + \frac{c_S\Gamma_1 + c_{AP}\Gamma_2}{\Gamma_1+\Gamma_3-\Gamma_2}[1-e^{-(\Gamma_1+\Gamma_3-\Gamma_2)\tau/2}] \\ c_P^* &= c_P + \frac{c_S\Gamma_3 + c_P\Gamma_4}{\Gamma_1+\Gamma_3-\Gamma_4}[1-e^{-(\Gamma_1+\Gamma_3-\Gamma_4)\tau/2}]. \end{aligned}$$

Consequently, we can numerically solve these simultaneous equations with respect to Γ_1 and Γ_3. The evaluated tunnel rates provide the corrected coefficients c_S, c_{AP}, and c_P, and their sum is nearly equal to 1 with the small deviation of 0.02. Therefore, it is confirmed that the above treatment can be used to obtain the accurate values of the coefficients and the tunnel rates.

APPENDIX E: NUMERICAL CALCULATION OF FCS IN PSB

For the numerical calculation of FCS, we follow the flow chart described in Fig. 11.

1. Compensation of tunnel rates for FCS

To reproduce the FCS numerically, we need to consider the compensation of the tunnel rates from the evaluated rates in Appendix D. In order to reconstruct the FCS shown in Fig. 2, it is necessary to consider the integration time of the digitizer and compensate the interdot tunnel rates. This integration time τ decides the resolution of the digitizer because the signal of the charge sensor measured from t to $t+\tau$ is averaged into

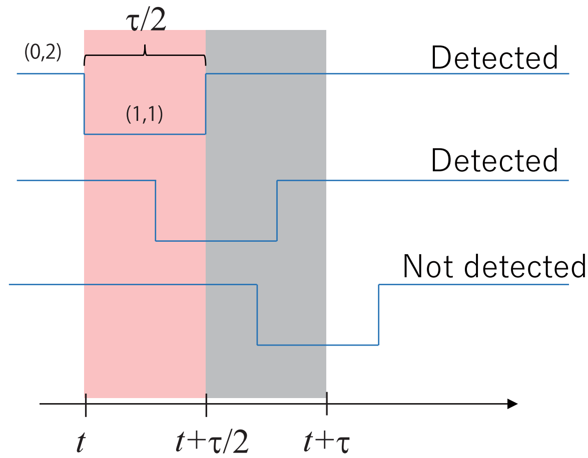

FIG. 12. Schematic of a typical signal at the (1,1) state for $\tau/2$ temporal width. The first two traces, which correspond to the interdot transition from (0,2) to (1,1) states in the red region, can be detected. In contrast, the interdot transition in the gray region cannot be detected.

one data point. As the integration time is not sufficiently short, some of the fast interdot transitions are not detected. First, we consider the sequential transition of the charge state: (0,2)⇒(1, 1) ⇒(0,2) [or (1,1)⇒ (0, 2) ⇒(1,1)], and assume that the transition is always counted when the waiting time Δt in the same state is longer than τ. Therefore, the expected value of count probability can be expressed as

$$\frac{\int_{\tau}^{\infty} e^{-\Gamma_i \Delta t} d\Delta t}{\int_{0}^{\infty} e^{-\Gamma_i \Delta t} d\Delta t}.$$

On the contrary, the sequential transition occurring within $\tau/2$ is not observed. However, if the waiting time (Δt) is $\tau/2$ or longer, the transitions can be partially detected with the probability $\Delta t/\tau$ because a threshold level of the charge sensor is set at the middle of the (0,2) and (1,1) charge states. Then, the expected value is given as

$$\frac{\int_{\tau/2}^{\tau} \frac{\Delta t}{\tau} e^{-\Gamma_i \Delta t} d\Delta t}{\int_{0}^{\infty} e^{-\Gamma_i \Delta t} d\Delta t}$$

The examples of sequential transitions that stay at the (1,1) state for $\Delta t = \tau/2$ are shown in Fig. 12. The first transition, which is the interdot transition from the upper to lower state in the red region, can be observed. However, the lowest trace, i.e., the transition occurring in the gray region cannot be detected.

Therefore, the compensation can be expressed as

$$\Gamma_i^* = \Gamma_i \frac{\left(\int_{\tau}^{\infty} e^{-\Gamma_i \Delta t} d\Delta t + \int_{\tau/2}^{\tau} \frac{\Delta t}{\tau} e^{-\Gamma_i \Delta t} d\Delta t\right)}{\int_{0}^{\infty} e^{-\Gamma_i \Delta t} d\Delta t} = \Gamma_i \left[\left(\frac{1}{2} + \frac{1}{\Gamma_i \tau} e^{-\Gamma_i \tau/2}\right) - \frac{1}{\Gamma_i \tau} e^{-\Gamma_i \tau}\right].$$

We chose τ =100 μs for the measurement, and Γ_i^* ($i = 1, 2, 3, 4$) is used for the numerical calculation of FCS in Fig. 2.

2. The detail of the numerical calculation

The numerical calculations are based on Eq. (1) in the main text. It can be easily shown that

$$P(\chi, t) = \exp(\mathcal{M}t) P(0, 0),$$

where $P(0, 0) = (P_S(0, 0), P_{AP}(0, 0), P_P(0, 0))^{\tau}$. It is convenient to introduce $\lambda \equiv e^{i\chi}$. Therefore,

$$\mathcal{M} = \begin{bmatrix} -(\Gamma_1 + \Gamma_3) & \Gamma_2\lambda & \Gamma_4\lambda \\ \Gamma_1\lambda & -\Gamma_2 & 0 \\ \Gamma_3\lambda & 0 & \Gamma_4 \end{bmatrix}.$$

$\exp(\mathcal{M}t)$ can be numerically evaluated to obtain FCS.

An approach for this evaluation includes the calculation of

$$\mathcal{K}(t, \Delta t) = (1 + \mathcal{M}\Delta t)^{t/\Delta t} \quad \text{(E1)}$$

for a sufficiently small time step Δt. $\mathcal{K}(t, \Delta t)$ is a matrix whose components are polynomials of λ. In numerical evaluation, we truncated them up to the 100th order of λ, because the probability that n interdot transitions occur in $t = 50$ ms almost vanishes for $n \geqslant 100$. We used $\Delta t = 5 \times 10^{-7}$s and verified that $\mathcal{K}(t, \Delta t)$ converges to $\exp(\mathcal{M}t)$ with a precision much higher than that limited by the statistical error of the experimental data.

To reduce the numerical multiplications of matrices, we performed the calculations as follows: $\mathcal{K}(t_1, \Delta t)$ was evaluated for $t_1 = 10^{-4}$ s using Eq. (E1); $\mathcal{K}(t_2, \Delta t)$ was then obtained for $t_2 = 10^{-3}$ s using

$$\mathcal{K}(t_2, \Delta t) = \mathcal{K}(t_1, \Delta t)^{t_2/t_1}.$$

This procedure was repeated for $t_3 = 10^{-2}$ s, $t_4 = 10^{-1}$ s, $t_5 = 1$ s, $t_6 = 10$ s, and $t_7 = 50$ s using

$$\mathcal{K}(t_n, \Delta t) = \mathcal{K}(t_{n-1}, \Delta t)^{t_n/t_{n-1}}.$$

[1] M. Field, C. G. Smith, M. Pepper, D. A. Ritchie, J. E. F. Frost, G. A. C. Jones, and D. G. Hasko, Phys. Rev. Lett. **70**, 1311 (1993).
[2] W. Lu, Z. Ji, L. Pfeiffer, K. W. West, and A. J. Rimberg, Nature **423**, 422 (2003).
[3] R. Schleser, E. Ruh, T. Ihn, K. Ensslin, D. C. Driscoll, and A. C. Gossard, Appl. Phys. Lett. **85**, 2005 (2004).
[4] L. M. K. Vandersypen, J. M. Elzerman, R. N. Schouten, L. H. W. van Beveren, R. Hanson, and L. P. Kouwenhoven, Appl. Phys. Lett. **85**, 4394 (2004).
[5] D. J. Reilly, C. M. Marcus, M. P. Hanson, and A. C. Gossard, Appl. Phys. Lett. **91**, 162101 (2007).
[6] A. Pioda, E. Totoki, H. Kiyama, T. Fujita, G. Allison, T. Asayama, A. Oiwa, and S. Tarucha, Phys. Rev. Lett. **106**, 146804 (2011).
[7] K. Kuroyama, M. Larsson, S. Matsuo, T. Fujita, S. R. Valentin, A. Ludwig, A. D. Wieck, A. Oiwa, and S. Tarucha, Sci. Rep. **7**, 16968 (2017).
[8] K. Kuroyama, M. Larsson, C. Y. Chang, J. Muramoto, K. Heya, T. Fujita, G. Allison, S. R. Valentin, A. Ludwig, A. D. Wieck,

S. Matsuo, A. Oiwa, and S. Tarucha, Phys. Rev. B **99**, 085203 (2019).
[9] O.-P. Saira, Y. Yoon, T. Tanttu, M. Möttönen, D. V. Averin, and J. P. Pekola, Phys. Rev. Lett. **109**, 180601 (2012).
[10] B. Küng, C. Rössler, M. Beck, M. Marthaler, D. S. Golubev, Y. Utsumi, T. Ihn, and K. Ensslin, Phys. Rev. X **2**, 011001 (2012).
[11] B. Küng, C. Rössler, M. Beck, M. Marthaler, D. S. Golubev, Y. Utsumi, T. Ihn, and K. Ensslin, J. Appl. Phys. **113**, 136507 (2013).
[12] J. V. Koski, A. Kutvonen, I. M. Khaymovich, T. Ala-Nissila, and J. P. Pekola, Phys. Rev. Lett. **115**, 260602 (2015).
[13] K. Chida, S. Desai, K. Nishiguchi, and A. Fujiwara, Nat. Commun. **8**, 15310 (2017).
[14] L. S. Levitov, H. Lee, and G. B. Lesovik, J. Math. Phys. **37**, 4845 (1996).
[15] D. A. Bagrets and Y. V. Nazarov, Phys. Rev. B **67**, 085316 (2003).
[16] S. Gustavsson, R. Leturcq, B. Simovič, R. Schleser, T. Ihn, P. Studerus, K. Ensslin, D. C. Driscoll, and A. C. Gossard, Phys. Rev. Lett. **96**, 076605 (2006).
[17] S. Gustavsson, R. Leturcq, B. Simovič, R. Schleser, P. Studerus, T. Ihn, K. Ensslin, D. C. Driscoll, and A. C. Gossard, Phys. Rev. B **74**, 195305 (2006).
[18] C. Flindt, C. Fricke, F. Hohls, T. Novotny, K. Netocny, T. Brandes, and R. J. Haug, Proc. Natl. Acad. Sci. USA **106**, 10116 (2009).
[19] T. Fujisawa, T. Hayashi, R. Tomita, and Y. Hirayama, Science **312**, 1634 (2006).
[20] V. F. Maisi, D. Kambly, C. Flindt, and J. P. Pekola, Phys. Rev. Lett. **112**, 036801 (2014).
[21] A. Kurzmann, P. Stegmann, J. Kerski, R. Schott, A. Ludwig, A. D. Wieck, J. König, A. Lorke, and M. Geller, Phys. Rev. Lett. **122**, 247403 (2019).
[22] P. Stano and P. Jacquod, Phys. Rev. Lett. **106**, 206602 (2011).
[23] F. Nichele, S. Hennel, P. Pietsch, W. Wegscheider, P. Stano, P. Jacquod, T. Ihn, and K. Ensslin, Phys. Rev. Lett. **114**, 206601 (2015).
[24] G. E. W. Bauer, E. Saitoh, and B. J. van Wees, Nat. Mater. **11**, 391 (2012).
[25] T. Hensgens, T. Fujita, L. Janssen, X. Li, C. J. V. Diepen, C. Reichl, W. Wegscheider, S. D. Sarma, and L. M. K. Vandersypen, Nature **548**, 70 (2017).
[26] D. C. Mattis, Int. J. Nanosci. **02**, 165 (2003).
[27] E. Nielsen and R. N. Bhatt, Phys. Rev. B **76**, 161202(R) (2007).
[28] A. Oguri, Y. Nisikawa, Y. Tanaka, and T. Numata, J. Magn. Magn. Mater. **310**, 1139 (2007).
[29] J. P. Dehollain, U. Mukhopadhyay, V. P. Michal, Y. Wang, B. Wunsch, C. Reichl, W. Wegscheider, M. S. Rudner, E. Demler, and L. M. K. Vandersypen, Nature **579**, 528 (2020).
[30] E. Manousakis, J. Low Temp. Phys. **126**, 1501 (2002).
[31] T. Byrnes, N. Y. Kim, K. Kusudo, and Y. Yamamoto, Phys. Rev. B **78**, 075320 (2008).
[32] K. Ono, D. G. Austing, Y. Tokura, and T. S., Science **297**, 1313 (2002).
[33] V. F. Maisi, A. Hofmann, M. Röösli, J. Basset, C. Reichl, W. Wegscheider, T. Ihn, and K. Ensslin, Phys. Rev. Lett. **116**, 136803 (2016).
[34] T. Fujita, P. Stano, G. Allison, K. Morimoto, Y. Sato, M. Larsson, J.-H. Park, A. Ludwig, A. D. Wieck, A. Oiwa, and S. Tarucha, Phys. Rev. Lett. **117**, 206802 (2016).
[35] A. Hofmann, V. F. Maisi, T. Krähenmann, C. Reichl, W. Wegscheider, K. Ensslin, and T. Ihn, Phys. Rev. Lett. **119**, 176807 (2017).
[36] J.-S. You, R. Schmidt, D. A. Ivanov, M. Knap, and E. Demler, Phys. Rev. B **99**, 214505 (2019).
[37] R. Hanson, L. P. Kouwenhoven, J. R. Petta, S. Tarucha, and L. M. K. Vandersypen, Rev. Mod. Phys. **79**, 1217 (2007).
[38] A. Beckel, A. Kurzmann, M. Geller, A. Ludwig, A. D. Wieck, J. König, and A. Lorke, Europhys. Lett. **106**, 47002 (2014).
[39] J. Danon, Phys. Rev. B **88**, 075306 (2013).
[40] R. Vyas and S. Singh, Phys. Rev. A **38**, 2423 (1988).
[41] M. Albert, G. Haack, C. Flindt, and M. Büttiker, Phys. Rev. Lett. **108**, 186806 (2012).
[42] G. Haack, M. Albert, and C. Flindt, Phys. Rev. B **90**, 205429 (2014).